Controlling the Formation Process of Methylammonium-Free Halide Perovskite Films for a Homogeneous Incorporation of Alkali Metal Cations Beneficial to Solar Cell Performance

Daming Zheng, Tao Zhu, Yanfa Yan, Thierry Pauporté

Cite this paper as: D. Zheng, T. Zhu, Y. Yan, Th. Pauporté, Adv. Energy Mater., (2022) 2103618. DOI:10.1002/aenm.202103618.

Controlling the formation process of Methylammonium-Free Halide Perovskite films for a homogeneous incorporation of alkali metal cations beneficial to solar cell performances

Daming Zheng[1], Tao Zhu[2], Yanfa Yan[2], Thierry Pauporté[1]**

1. Chimie ParisTech, PSL Research University, CNRS, Institut de Recherche de Chimie Paris (IRCP), UMR8247, 11 rue P. et M. Curie, F-75005 Paris, France.
2. Department of Physics and Astronomy and Wright Center for Photovoltaics Innovation and Commercialization, University of Toledo, Toledo, OH, USA.

* Authors for the correspondence. E-mails: Yanfa.Yan@utoledo.edu; thierry.pauporte@chimieparisrech.psl.eu
Website: www.pauportegroup.com

KEYWORDS: Solar cells, Film formation control and mechanism, Multi-alkali metal cation, Glow discharge Optical Emission Spectroscopy, Methylammonium-free perovskite

Abstract

Incorporating multiple cations of the IA alkali metal column of the periodic table ($K^+/Rb^+/Cs^+$) to prepare perovskite films is promising for boosting the photovoltaic properties. However, contrary to K^+, both Cs^+ and Rb^+ suffer from non-uniformity at the origin of performance and stability losses. In this paper, Ammonium chloride (NH_4Cl) additive is shown to address this concern. We analyze step-by-step the effects of NH_4Cl Additive and Alkali Metal Cations ($K^+/Rb^+/Cs^+$) on the one-step film formation process of methylammonium-free, formamidinium-based, halide perovskites. First, we highlight the action of NH_4Cl additive on the spin-coating and the anti-solvent dripping processes. We show that it improves the solubility of PbI_2 in solution by forming an intermediate and then favor the perovskite phase formation. Then, we investigate the annealing process, showing the increased grain size, improved crystallinity and PbI_2 suppression by adding NH_4Cl.

Cite this paper as: D. Zheng, T. Zhu, Y. Yan, Th. Pauporté, Adv. Energy Mater., (2022) 2103618. DOI:10.1002/aenm.202103618.

Moreover, by introducing depth profile evolution monitoring by the glow discharge optical emission spectroscopy (GD-OES) technique, we visualize the real-time distribution changes of multi-alkali metal cations (m-AMCs) in the film upon annealing at 155°C. We show that K at low concentration is homogeneously distributed throughout the film. Cs is more concentrated at the surface and Rb in the film depth. With NH_4Cl additive, these two alkali metals are more homogeneously distributed. We show that NH_4Cl can slow down the movement of m-AMCs so that they are better evenly distributed into the perovskite layer. Moreover, it changes the growth direction of the perovskite film, making the overall crystallization quality improved and the distribution more uniform. It results in perovskite films with large monolithic grains, permitting a high stabilized power conversion efficiency (PCE) over 21%. Finally, by combining AC additive and film surface treatment with n-propylammonium iodide (PAI), the performance was further upgraded at a stabilized PCE of 22.04%.

1. Introduction

During the past decade, organo-metal halide perovskites (PVKs) have risen as the most promising semiconductor family for photovoltaic devices due to a broad range of unique properties.[1-11] The present record power conversion efficiency (PCE) for a perovskite solar cell (PSC) is 25.7%.[12] However, PSCs still need further progress to overcome instability issues caused by moisture, oxygen, and heat, while maintaining or improving their PCE. The composition of ABX_3 based 3D hlide perovskite greatly affects the overall performance of perovskite solar cells. Different components can bring desired properties, such as improved optical properties or structural stability. To achieve better performance of PSC, perovskite materials composition has been complexified by combining several A^+ monovalent elemental and organic cations, from double-cation (*e.g.* MA-FA,[13,14] Cs/FA,[15,16] Rb/FA,[17] MA^+ being methylammonium and FA^+ being formamidinium) to triple-cation (*e.g.* Cs/MA/FA,[8,18,19] Rb/MA/FA,[20] K/Cs/FA[21]), and quadruple-cation (Rb/Cs/MA/FA[18,22]). The incorporation of other cations, namely MA^+, Cs^+, Rb^+ and K^+, aims at alleviating the formation of photo inactive δ-$FAPbI_3$ phase and/or suppress defects in perovskite film. Although MA-based perovskite solar cells can achieve very high PCE,[23-25] the presence of MA can favor PVK degradation since MA is easily released and decomposed under heating and humid atmosphere. A lot of works have been dedicated to enhancing the stability of the black α-$FAPbI_3$ phase, notably to its entropic stabilization by incorporating Cs.[18,19] The structural engineering by introducing elemental monovalent cations can shed light on the long-term stability of PSCs. For instance, introducing another alkali metal, Rb (same column as Cs and K), into $FAPbI_3$ perovskite has been shown to enhance both the photovoltaic performance and the moisture stability.[17] Moreover, the nonradiative loss and photoinduced ion migration in perovskite film is significantly reduced by using potassium halide to

Cite this paper as: D. Zheng, T. Zhu, Y. Yan, Th. Pauporté, Adv. Energy Mater., (2022) 2103618. DOI:10.1002/aenm.202103618.

passivate the defects at near surface and grain boundaries.[26] All these considerations led us to develop multi-alkali metal cations (m-AMCs) $KRbCsFAPbI_3$ 3D perovskites. However, phase segregation might happen on m-AMCs perovskite films and the distribution of each element is worth noting. Especially, the homogeneous distribution of Rb^+ is sought for high stability and performances.[27]

In our previous work,[16] we proved that using ammonium chloride (NH_4Cl, noted AC) as an additive effectively improves the efficiency of solar cells based on CsFAPI absorbing layer. As far as we know, only a few works tentatively explain the mechanism of action of ammonium chloride. Among them, Chen and co-workers[28] added ammonium chloride as an additive to $MAPbI_3$ by using a surface-activation chemical vapor deposition process (SA-CVD) and provided the corresponding mechanism in their paper. Another work by Qi and co-worker[29] used a two-step process to prepare $Cs_{0.05}FA_{0.54}MA_{0.41}Pb(I_{0.98}Br_{0.02})_3$ layers. In their work, ammonium chloride was first mixed with PbI_2 and spin-coated on the substrate, and then a mixed solution of FAI and CsI was dripped on the substrate to form the perovskite layer. The obtained perovskite films had large grain size, which was ascribed to the AC introduced intermediate phase. AC has been shown by Rong et al.[30] to assist the crystallization of $MAPbI_3$ perovskite in ambient air by the formation of a hydrate intermediate compound which forms high-quality perovskite crystals by decomposition under ambient conditions. In the present paper, we examine in-depth how NH_4Cl additive works at each stage of the so-called one-step preparation of perovskite films to elucidate its action mechanism and we associate it with the film formation process of m-AMCs perovskites. We have visualized the distribution and moving trajectory of m-AMCs. Moreover, a systematic study of the effect of AC and potassium iodide on the distribution of m-AMCs has been conducted by using glow discharge-optical emission spectroscopy (GD-OES). Based on the multiple advantages of this techniques (a high detection limit (10 μg/g), the depth profile analysis (through a thickness up to 100 μm) and the large detection area (tens square millimeters)) we have been able to track the composition of the entire perovskite layer at every moment of their preparation process. Consequently, we have obtained the movement trajectory of the AMCs during the film formation process by detecting the depth distribution of multiple metal cations in the perovskite film upon thermal annealing at various times. We show that the addition of AC makes the distribution of the multi-element cationic metal ions in the entire perovskite layer more uniform. The film quality of the perovskite layer is significantly improved. One important discovery is that the crystallization/growth direction change from top-down to lateral with the NH_4Cl additive, making Rb^+ evenly distributed in the perovskite film. Finally, the overall performance of PSCs is greatly improved, and the champion device power conversion efficiency (PCE) reaches 22.5% (stabilized at 22.04 %).

Cite this paper as: D. Zheng, T. Zhu, Y. Yan, Th. Pauporté, Adv. Energy Mater., (2022) 2103618. DOI:10.1002/aenm.202103618.

2. Results and Discussion

2.1 Solar cell performances and optimization

The effect of Cs content in $FAPbI_3$ was investigated in our previous work,[21] where we found an optimal doping ratio of 10% to form the $Cs_{0.10}FA_{0.90}PbI_3$ perovskite (noted CsFA hereinafter). Furthermore, the beneficial effect of adding a small amount of Rb into CsFAPI was reported in the literature,[31,32] with an optimal doping ratio of 5% that we have retained in the present work to form the $Rb_{0.05}Cs_{0.10}FA_{0.85}PbI_3$ perovskite (noted RbCsFA hereinafter). Then, the influence of the addition of KI on the performance of the perovskite solar cell investigated and the optimum the amount of this metal halide was found at 5% (the details of this study are reported in **Part A**, Supporting Information). Moreover, we systematically studied ammonium chloride (AC) additive at concentrations varying between 10 and 40 mol% of molar PbI_2 content in the $K_{0.05}Rb_{0.05}Cs_{0.10}FA_{0.80}PbI_3$ precursor solution. We proved that 30 mol% is the optimal addition amount. These layers and solar cells are noted KRbCsFA hereinafter and the optimization study is detailed in **Part B (**Supporting Information). This result is consistent with other optimization results we got in our previous work on other methylammonium-free perovskites.[21]

Table 1. Champion solar cells *J-V* curve parameters, PCE and hysteresis index.

Name	Additive	Capping layer	Scan direction	V_{oc} [V]	J_{sc} [mA. cm^{-2}]	*FF*	PCE [%]	*HI*[a)] [%]
CsFA	NO	NO	Reverse	0.943	23.91	72.13	16.26	26
			Forward	0.846	23.83	59.36	11.96	
RbCsFA	NO	NO	Reverse	1.017	24.49	76.12	18.96	24
			Forward	1.006	24.36	58.89	14.43	
KRbCsFA	NO	NO	Reverse	1.031	23.96	78.08	19.29	3
			Forward	1.034	23.79	76.17	18.74	
KRbCsFA /AC	NH_4Cl 30 mol%	NO	Reverse	1.083	24.79	78.61	21.10	4
			Forward	1.072	24.66	76.74	20.29	
KRbCsFA /AC-PAI	NH_4Cl 30 mol%	YES	Reverse	1.121	24.86	80.83	22.53	4
			Forward	1.116	24.71	78.84	21.74	

[a)] Hysteresis Index noted HI, defined as $(PCE_{Rev}-PCE_{For})*100/PCE_{Rev}$

Cite this paper as: D. Zheng, T. Zhu, Y. Yan, Th. Pauporté, Adv. Energy Mater., (2022) 2103618. DOI:10.1002/aenm.202103618.

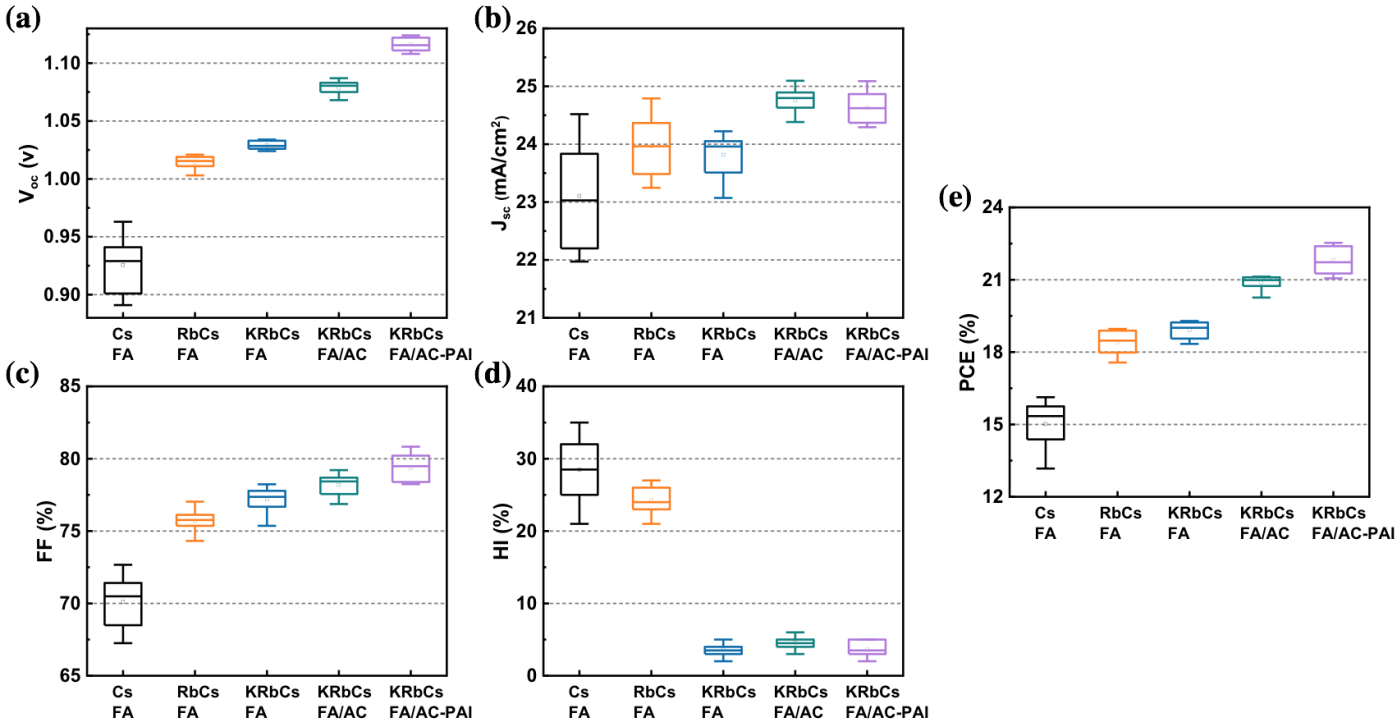

Figure 1. Statistical analysis of the optimized PSCs *J-V* curve parameters and PCE.

Table 1 and **Figure S7** (Supporting Information) summarize the best cells results and the overall situation of different *J-V* curves parameters for the investigated PSCs. Their statistical analysis is displayed in **Figure 1**. The CsFA cells exhibited poor performances with a *PCE* at 16.2 % on the reverse scan (**Figure S7a**, Supporting Information) and a large hysteresis (**Table 1**). After introducing Rb ions, all the photovoltaic parameters were enhanced, especially the *FF* and the V_{oc} (**Figure 1**). However, RbCsFA perovskite solar cells kept a large *HI*, which will directly cause a low stabilized PCE. We then introduced KI in the perovskite precursor solution (PPS) to decrease the *HI* parameter and to increase the stabilized PCE. In our previous work,[16] we have directly related the blocking of the iodide ion movement and the introduction of potassium ions (from KCl). We have deduced that it is the result of native defect passivation by potassium. This blocking is correlated with the reduction of the *HI* parameter.[16] The actual results are indeed the same as our predictions. By incorporating KI in the PPS, the *HI* is decreased from 26% to 3%. Moreover, the external quantum efficiency (*EQE)* spectra are reported in **Figure S8** (Supporting Information), and their integration results are in good agreement with the J_{sc} of the devices. In the following, we have done a detailed analysis of the effect of the AC additive on the film formation and we give its detailed action mechanism. We will see that AC acts by forming AC related intermediates and that it makes the distribution of metal cations more uniform. Based on the various benefits given by the additives, the final *PCE* of the KRbCsFA/AC sample achieved 21.1% with negligible hysteresis. In **Figure S9** (Supporting Information), we present the *PCE* trackings at the maximum power and corresponding steady-state *PCEs*. It is noted that the KRbCsFA device with potassium has a better *PCE* compared to RbCsFA device, despite efficiencies,

Cite this paper as: D. Zheng, T. Zhu, Y. Yan, Th. Pauporté, Adv. Energy Mater., (2022) 2103618. DOI:10.1002/aenm.202103618.

measured on the reverse *J-V* scans, that are almost the same (**Table 1**). From **Figure 1**, we confirm that AC can enhance all the performance parameters of solar cells. Finally, the best steady-state *PCE* was reached for the KRbCsFA/AC device due to the synergistic action of potassium ion and ammonium chloride. Eventually, by using n-propylammonium iodide (PAI) post-treatment, the stability and performance were further enhanced with a stabilized PCE at 22.04 % (**Figure S9,** Supporting Information**).**

2.2 Characterizations of the films

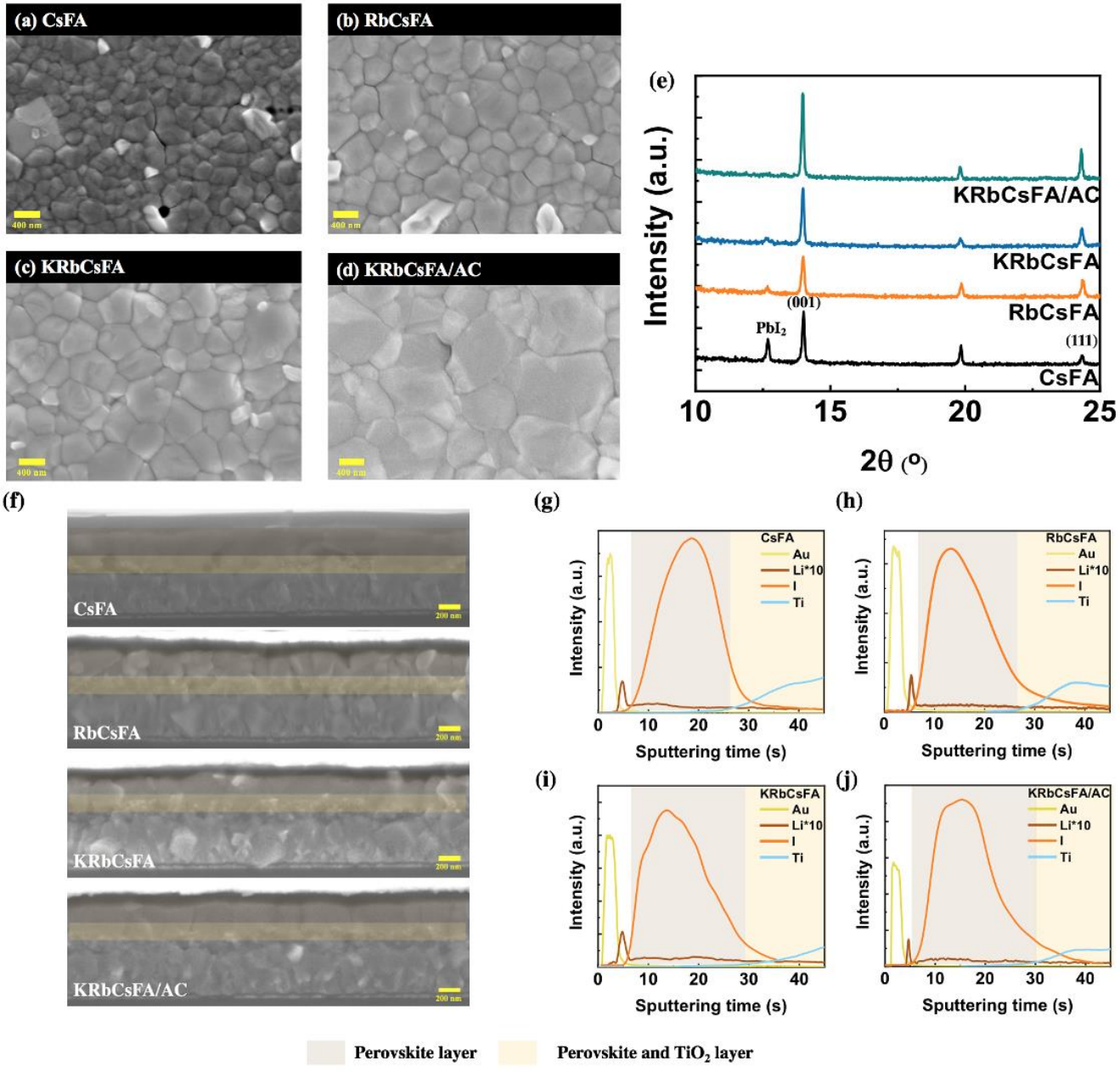

Figure 2. (a-d) SEM top views of the investigated perovskite layers. (e) XRD patterns of these four kinds of perovskite layers. (f) SEM cross-sectional views of perovskite layers deposited on glass/FTO/*c*-TiO_2/*mp*-TiO_2

and topped with a Spiro-OMeTAD layer (the yellow part outlines *c*-TiO_2/*mp*-TiO_2). (g-j) Element distribution across the entire devices measured by GD-OES: g) CsFA cell, h) RbCsFA cell, i) KRbCsFA cell, and j) KRbCsFA with AC cell.

We first focused our attention on the morphology of the perovskite layers. From **Figure 2a** to **2c**, we can see that the incorporation of more kinds of alkali metal cations improved the morphological quality of the films, which manifested itself by the increase of grain size, elimination of the pinholes, and the decrease of lead iodide crystals (bright grains), especially present on the surface. The mean grain size of RbCsFA and KRbCsFA were very close, around 730 nm, much larger than 327 nm for the CsFA sample (**Figure S10a**, Supporting Information). The reduction of lead iodide crystal content means that more of PbI_2 is converted into perovskite crystals. XRD results in **Figure 2e** confirm this conclusion. With the increased kinds of AMCs incorporated, the (001) perovskite peak gradually increased, while the intensity of PbI_2 at 12.6 ° gradually weakened. In addition, compared to samples without additives, the sample with AC as the additive presented a larger grain size, as shown in **Figure 2d**. The addition of AC significantly increased the grain size from 730 nm to 1100 nm. XRD results show that it went along with an increase in the material crystallinity (**Figure 2e**). While increasing the crystal size with an increase in AMCs, we found from the XRD results that the peaks at (001) and (002) moved to the left, which means that the perovskite lattice also expanded. The displacement amplitude of (002) is larger than (001) in **Figures S10b** and **S10c** (Supporting Information), which can be explained as peak shift is usually more apparent at larger angles.[33] The shift of the perovskite peak can have two origins. Due to the small ionic radii of Rb^+ (152 pm) and K^+ (133 pm) compared to FA^+ (253 pm) they can hardly act directly as substitutes into the lattice.[26] Expansion would indicate iodide taking-up interstitial position assisted by metal cation. Lattice expansion can also be induced by strain in the layer. Strain could explain for instance the lattice expansion of KRbCsFA sample prepared with AC additive (**Figure S10**, Supporting Information).

Changes in lattice constant usually lead to changes in the bandgap. The optical properties of the perovskite films were characterized by UV-VIS spectroscopy and photoluminescence (PL) spectroscopy. The absorbance spectra in **Figure S11** (Supporting Information) show that absorption onset of RbCsFA, KRbCsFA and KRbCsFA/AC samples are red-shifted compared to the CsFA sample. The bandgap of CsFA, RbCsFA, KRbCsFA and KRbCsFA/AC samples are estimated to be 1.550 eV, 1.540 eV, 1.535 eV and 1.538 eV, respectively (**Figure S12**, Supporting Information). The bandgap reduction agreed with the steady-state PL spectra of these films (**Figure S11b,** Supporting Information). We also observed a redshift in the emission peak of the KRbCsFA sample (814 nm) compared to the RbCsFA sample (811 nm) and the CsFA sample (805 nm).

In **Figure 2f**, the results of cross-sectional SEM characterizations further verify the conclusion from XRD and shows the monolithic morphology of the KRbCsFA/AC layer. In a next step, we measured

Cite this paper as: D. Zheng, T. Zhu, Y. Yan, Th. Pauporté, Adv. Energy Mater., (2022) 2103618. DOI:10.1002/aenm.202103618.

the compositional profile of the full cells and investigated the effect of grains growth conditions on these profiles. GD-OES allowed us to conspicuously distinguish the various layers composing the solar cells. We followed the main inorganic elements of the structure, namely Au, Li, I and Ti. In **Figures 2g-j**, they appeared successively at increasing Ar sputtering time. One can note that the relative intensity of the various elements does not correspond directly to the relative concentrations due to the independent sputtering and emission yields for each element. First, Au of the back-electrode appeared. Then we observed a sharp Li peak corresponding to the dopant in the Spiro-OMeTAD organic hole transporting layer. This organic layer was etched rapidly. The signal of Li, present in small quantity, is multiplied by 10 in **Figures 2g-j**. Then the perovskite layer appeared after 7s of sputtering time with the presence of I. After the 26s-30s, Ti of TiO_2 appeared.

2.3 Film formation mechanism

The above-described final films properties result from the film formation process which is greatly influenced by the additives and multiple alkali metal cations. Three major issues about the mechanisms must be understood now and linked together: 1) The role of NH_4Cl on the film formation of perovskites containing m-AMCs; 2) The m-AMCs distribution change during the film formation process; 3) The effect of additives on the formation direction of perovskite films upon annealing.

2.3.1 The role of NH_4Cl on the film formation

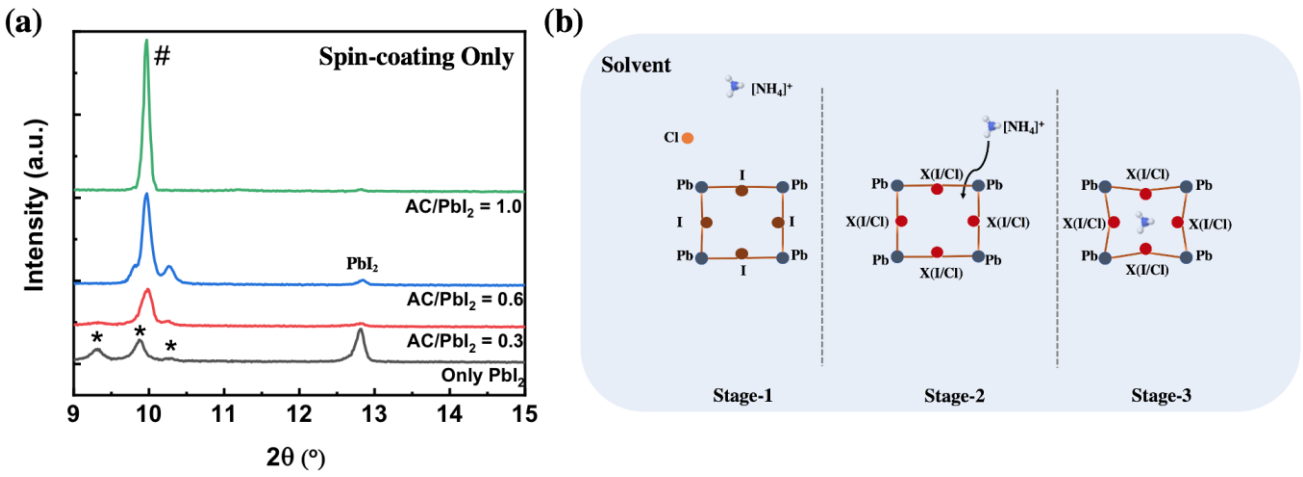

Figure 3. (a) XRD patterns of films formed by spin-coating solutions with different ratios of ammonium chloride versus PbI_2 (no dripping). (b) Intermediate $[NH_4]_x^+$ $[PbI_2Cl_x]^{x-}$ formation process. (*****: Pb-I-solvent intermediate; **#**: $[NH_4]_x^+$ $[PbI_2Cl_x]^{x-}$).

To get a comprehensive understanding of how AC impacts the process of perovskite film formation, we first studied by XRD the behavior of NH_4Cl and PbI_2 combinations. This allowed us to exclude interference with other cations. According to **Table S2** (Supporting Information) and the above

Cite this paper as: D. Zheng, T. Zhu, Y. Yan, Th. Pauporté, Adv. Energy Mater., (2022) 2103618. DOI:10.1002/aenm.202103618.

discussion, we know that the best amount of AC to get the highest PCE is 30 mol% of PbI_2. We first investigated films obtained by spin-coating only (no dripping of anti-solvent) three different AC to PbI_2 molar ratio (0.3, 0.6 and 1) mixtures in DMF/DMSO solvent. In **Figure 3a**, one can distinguish the PbI_2 diffraction peak at 12.6 ° along with three peaks between 9 ° and 10.5 °. According to Ref.[34], the latter belong to the Pb-I-solvent system. The intensity of the crystal PbI_2 peak was strong in the sample without AC. It means that PbI_2 remained in the solution as small crystallites because it did not completely dissolve in the DMF/DMSO solvent this case. With the increasing amount of AC added to PbI_2 solution, the peaks at 12.6 ° gradually disappeared. It indicates that AC increases the solubility of PbI_2. Moreover, the 9.32 °and 10.28 ° peak were also progressively reduced, showing that all Pb-I-solvent related intermediates converge into an unique one. Among the Pb-I-solvent related three intermediate peaks in **Figure 3a**, the main peak at 9.86 ° moved to 9.97 ° after we added AC into PbI_2 solution, therefore the lattice is shrunk because NH_4^+, with a small ionic radius, preferentially diffuses into the $[PbI_2Cl_x]^{x-}$ octahedral layer and form an $[NH_4]_x^+$ $[PbI_2Cl_x]^{x-}$ intermediate phase (**Figure 3b** and **Reaction (1)**). Since we did not detect the existence of these intermediates in the XRD results in each step of the preparation process for all kinds of samples (**Figures S13-S15**, Supporting Information), we firmly believe that this intermediate forms before (α-)δ-phase (**Reaction (3)**) and acts as an intermediate which favors the formamidinium lead iodide formation (**Reaction (2)**). Another reason is that, AC and PbI_2, easily react together, even in powder mixtures as shown in Ref. [30]. It indicates that the energy required for the reaction is shallow. In **Figure 3b**, we describe the process of $[NH_4]_x^+$ $[PbI_2Cl_x]^{x-}$ intermediate phase formation.

$$\mathbf{PbI_2 + xNH_4Cl \rightarrow [NH_4]_x^+[PbI_2Cl_x]^{x-}} \quad \mathbf{(1)}$$

$$\mathbf{[NH_4]_x^+[PbI_2Cl_x]^{x-} + FAI \rightarrow (\alpha\text{-})\delta\text{-}FAPbI_3 + xNH_4Cl} \quad \mathbf{(2)}$$

$$\mathbf{PbI_2 + FAI \rightarrow (\alpha\text{-})\delta\text{-}FAPbI_3} \quad \mathbf{(3)}$$

Finally, the PSC results have shown an optimum amount of AC at 30 %, while more AC favors the PbI_2 dissolution. We prepared layers from the four PbI_2/AC solutions already used in **Figure 3a**, following the full perovskite preparation protocol (including dripping and annealing). The final layers were all made of PbI_2 because NH_4^+ was eliminated by heat. Their morphologies are reported in **Figure S13** (Supporting Information). We see that excessive AC leads to crystal overlaps. This kind of crystal overlap causes uncontrolled growth of PbI_2 and then increases the number of pinholes and defects that are detrimental for the devices (**Figures S16d** and **S16e**, Supporting Information). We can suppose that a similar behavior occurs in the presence of FAI and m-AMC and it is why AC amount must not be too high.

The above-detailed analysis has clarified the mechanism of AC action on PbI_2. To better understand the effect of m-AMCs and AC on the film formation process, we subsequently used XRD to track and analyze the crystallization at each stage of the "one-step" preparation for the various m-AMCs

Cite this paper as: D. Zheng, T. Zhu, Y. Yan, Th. Pauporté, Adv. Energy Mater., (2022) 2103618. DOI:10.1002/aenm.202103618.

perovskite films. Moreover, we propose in **Part D** of the Supporting Information, after a detailed study, the reactions occurring, with and without AC, at the three successive layer preparation stages: spin-coating, anti-solvent dripping and film annealing.

2.3.2 Elements distribution upon the annealing film process

We introduced GD-OES as a powerful measurement technique to gain the depth-profile distribution of the cations upon the film formation process focusing on the annealing step. As far as we know, this work is the first reporting the real-time moving track of m-AMCs upon the film-formation process.

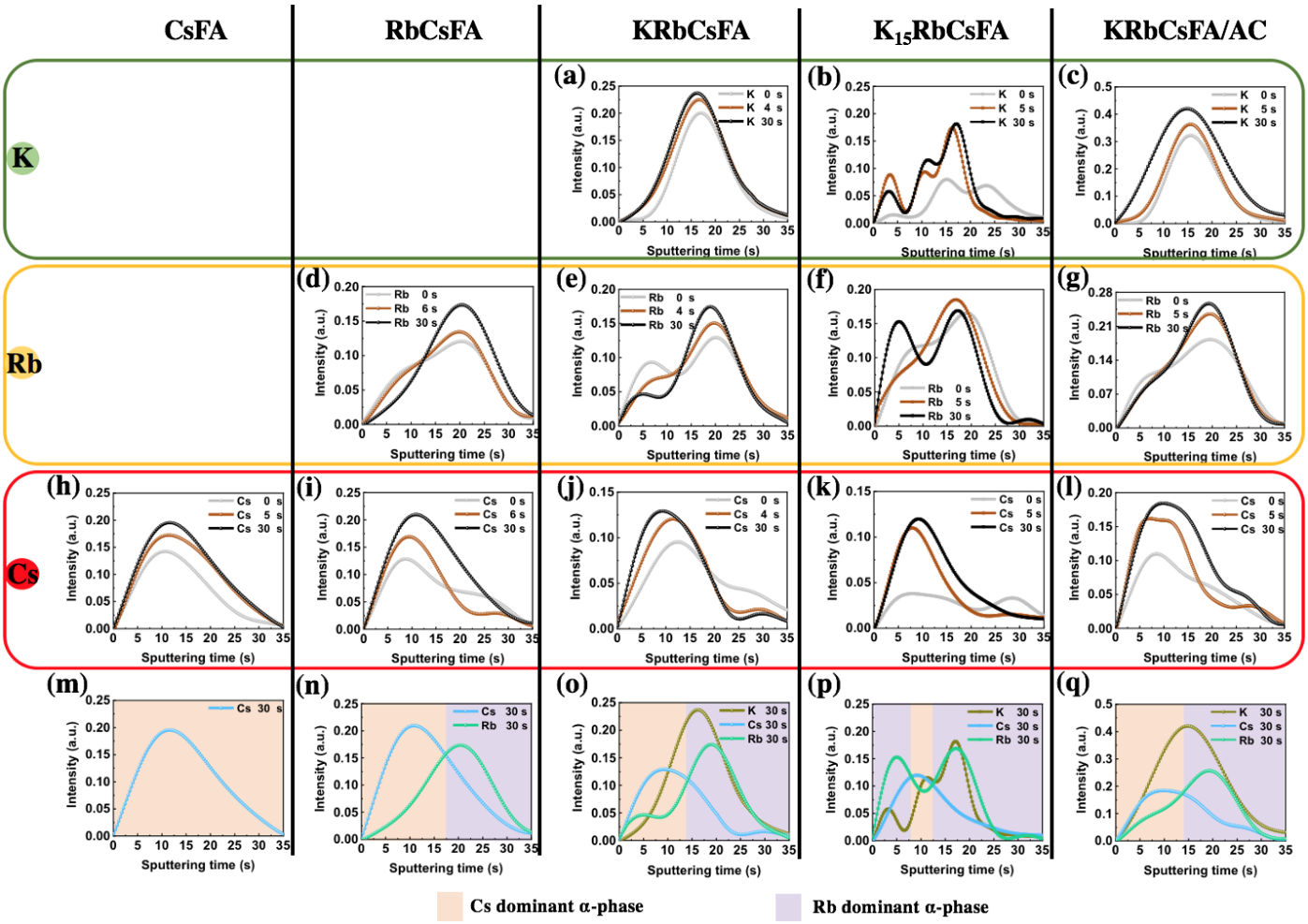

Figure 4. Distribution profiles of different metal cations upon annealing by using GD-OES. (a-c) Distribution of potassium ions. (d-g) Distribution of rubidium ions. (h-l) Distribution of cesium ions. (m-q) All metal ion profiles after annealing for 30s, (m) CsFA, (n) RbCsFA, (o) KRbCsFA, (p) K_{15}RbCsFA ($K_{0.15}Rb_{0.05}Cs_{0.10}FA_{0.70}PbI_3$), (q) KRbCsFA/AC.

Figure 4 presents the profile evolution upon annealing for five kinds of m-AMCs perovskite compositions. When only cesium ions were present in CsFA samples, the curve strength of cesium ions increased and became boarder with the increase of annealing time (**Figure 4h**). This means that with

Cite this paper as: D. Zheng, T. Zhu, Y. Yan, Th. Pauporté, Adv. Energy Mater., (2022) 2103618. DOI:10.1002/aenm.202103618.

the increasing annealing time, phase transition and continuous solvent evaporation, Cs gradually enters into the δ-$FAPbI_3$ lattice. Then the corresponding crystallinity of the film becomes higher, which makes the distribution of Cs in the perovskite film more uniform from top to bottom. For the RbCsFA sample, which contains two AMCs, we found that the distribution of Rb and Cs was not uniform in the perovskite layer and showed two peaks before annealing. When the annealing time increased from 0 to 30s, the Rb curve gradually moved in the direction of the TiO_2 layer (**Figure 4d**), while Cs moved in the opposite direction (**Figure 4i**). The reason for the upward movement of Cs may be due to a large amount of solvent evaporation at the surface of the perovskite layer upon annealing, which first causes crystallization on the surface. The energy required for the formation of Cs dominant α-phase is lower than the formation of Rb dominant α-phase, so the moving direction of Cs is upwards. From the perspective of the energy required for phase transformation, the temperature needed for all-inorganic perovskite $CsPbI_3$ to transform from orthorhombic (δ-phase) to a cubic (α-phase) structure is 300 °C,[36,37] but $RbPbI_3$ cannot convert from yellow phase to black phase even at its melting point.[38] In **Figure 4n**, on the one hand, we can see that the intensity of Rb is very low from 0 to 10 seconds (sputtering time), but the intensity of Rb gradually increases after 10 seconds (sputtering time). We can also see from **Figure S17c** (Supporting Information) that until the end of the annealing process, the peak of Rb does not move much, which is because Rb is mainly concentrated in the bulk perovskite rather than on the surface of the perovskite.[27] On the other hand, from the beginning to the end, the curves of Cs and Rb always have overlapping areas. This indicates that it is not just superposition of CsFA and RbFA, but perfect integration into lattice and grain boundary of the perovskite.

For the KRbCsFA sample, which contains three AMCs, potassium ions are homogeneously distributed throughout the perovskite layer as potassium has a small atomic radius (**Figure 4a**). From 0 seconds to 30 seconds of annealing time, there are always two peaks of Cs and Rb, which means that these two elements are non-uniformly distributed in the perovskite layer. For Rb, the concentration is lower in the perovskite's upper layer than in the lower part of the layer (**Figure 4e**). The distribution of cesium is opposite to that of rubidium (**Figure 4j**). It should be noted that the position of the first peak and the second peak of the Cs curve in **Figure 4j** are discontinuous, which indicates that the Cs element fault appears at the interface between the perovskite and TiO_2 layer but is re-enriched in the TiO_2 layer. By comparing the recipe with and without potassium ion, we can find that, after adding potassium ion in the PPS, the peak intensity of Rb and Cs changes little at the same time after ~5 s of annealing. This also shows that the addition of potassium ions accelerates the movement of AMCs during annealing, which means that the energy required for film formation is reduced (**Figure S18**, Supporting Information). We will verify this point in the differential Scanning Calorimetry (DSC) results what will be discussed below. Compared with RbCsFA showed in **Figure 4n**, the distribution of Cs and Rb in **Figure 4o** is less uniform, and the peak of Cs shifts to the left by 4 seconds (sputtering time). Although the Rb curve has a small peak at 5s, the curve is still continuous and does not fluctuate much. The presence of potassium ions seems to enable Cs and Rb to be better integrated in the upper part of the perovskite layer. We need to mention that these m-AMCs do not move significantly during

Cite this paper as: D. Zheng, T. Zhu, Y. Yan, Th. Pauporté, Adv. Energy Mater., (2022) 2103618. DOI:10.1002/aenm.202103618.

the annealing period from 30 s to 15 min (**Figure S17**, Supporting Information). For this reason, the graph we show in **Figure 4n-q** is only 30 seconds.

As for the recipes with AC, all AMCs distribution became more even than the sample without AC, especially the distribution of Rb. On the one hand, these m-AMCs show broader peaks (**Figures 4c**, **4g** and **4l**). On the other hand, compared to the double peaks of Rb and Cs in the KRbCsFA sample (**Figures 4e** and **4j**), there are no prominent double peaks in the KRbCsFA/AC sample. Two possible reasons can explain the more uniform distribution of these m-AMCs: 1) It seems that AC can slow down the movement of m-AMCs so that they can be better evenly distributed into the perovskite layer; 2) The growth direction of perovskite film changes, which improves the overall crystallization quality and makes the distribution more uniform.

It must be emphasized here that this kind of broad and homogeneous distribution in m-AMCs containing perovskites exhibit a better stability compared to the fluctuating ones. **Figure S19** (Supporting Information) shows the stability of these four kinds of perovskite layers after aging for 5 hours under very high humidity conditions (90±5% RH). In this accelerated stability test, the results for an aging time of five hours reflected the stability for these four different compositions and recipes under high humidity. Compared with CsFA and KRbCsFA, the RbCsFA major degradation product is PbI_2 and not the yellow δ-phase. The case of the CsFA sample is just the opposite to that of the RbCsFA sample with an being easier transformation into a yellow δ-phase. The presence of Rb also helps stabilize the α-phase. For aging, a phase transition is preferable rather than the decomposition of perovskite crystals. However, for a sample doped with potassium ion, the decrease in the intensity of the (001) peak is accompanied by the enhancement of the δ-phase peak. At the same time, a new peak around 9.4 ° appears, which belongs to the δ-$CsPbI_3$.[39] It indicates that the phase separation is more likely to occur for the KRbCsFA sample under high humidity. The fantastic point is that the KRbCsFA/AC sample presents a very high stability compared to the other samples with very weak δ-phase and PbI_2 signals after the aging experiment. The reason for this is a better crystallization with a more uniform distribution of m-AMCs, especially the distribution of Rb that can better stabilize the α-phase.

We also explored the phase separation phenomenon in the potassium-rich $K_{0.15}Rb_{0.05}Cs_{0.10}FA_{0.70}PbI_3$ (noted K_{15}RbCsFA) sample. Compared with the potassium-poor KRbCsFA sample, the GD-OES curve of K_{15}RbCsFA showed multi-peak distributions for the K and Rb curves (**Figures 4b** and **4f**). This result of uneven distribution in **Figure 4p** explains well the (002) peak of δ-$CsPbI_3$ at around 10 ° found in **Figure S1e** (Supporting Information).[40] The excessive potassium causes an extremely uneven distribution of other AMCs in the perovskite layer during the film formation process and finally leads to phase segregation, as shown in **Figure 4p**. Consequently, the results obtained by GD-OES show the distribution of m-AMCs in the perovskite layer under phase separation. In addition, we can surely say that the atomic ratios corresponding to different depths of the m-AMCs contained perovskite layer are not the same, that is they change with the depth.

Cite this paper as: D. Zheng, T. Zhu, Y. Yan, Th. Pauporté, Adv. Energy Mater., (2022) 2103618. DOI:10.1002/aenm.202103618.

2.3.3 Solvent elimination and film growth upon annealing.

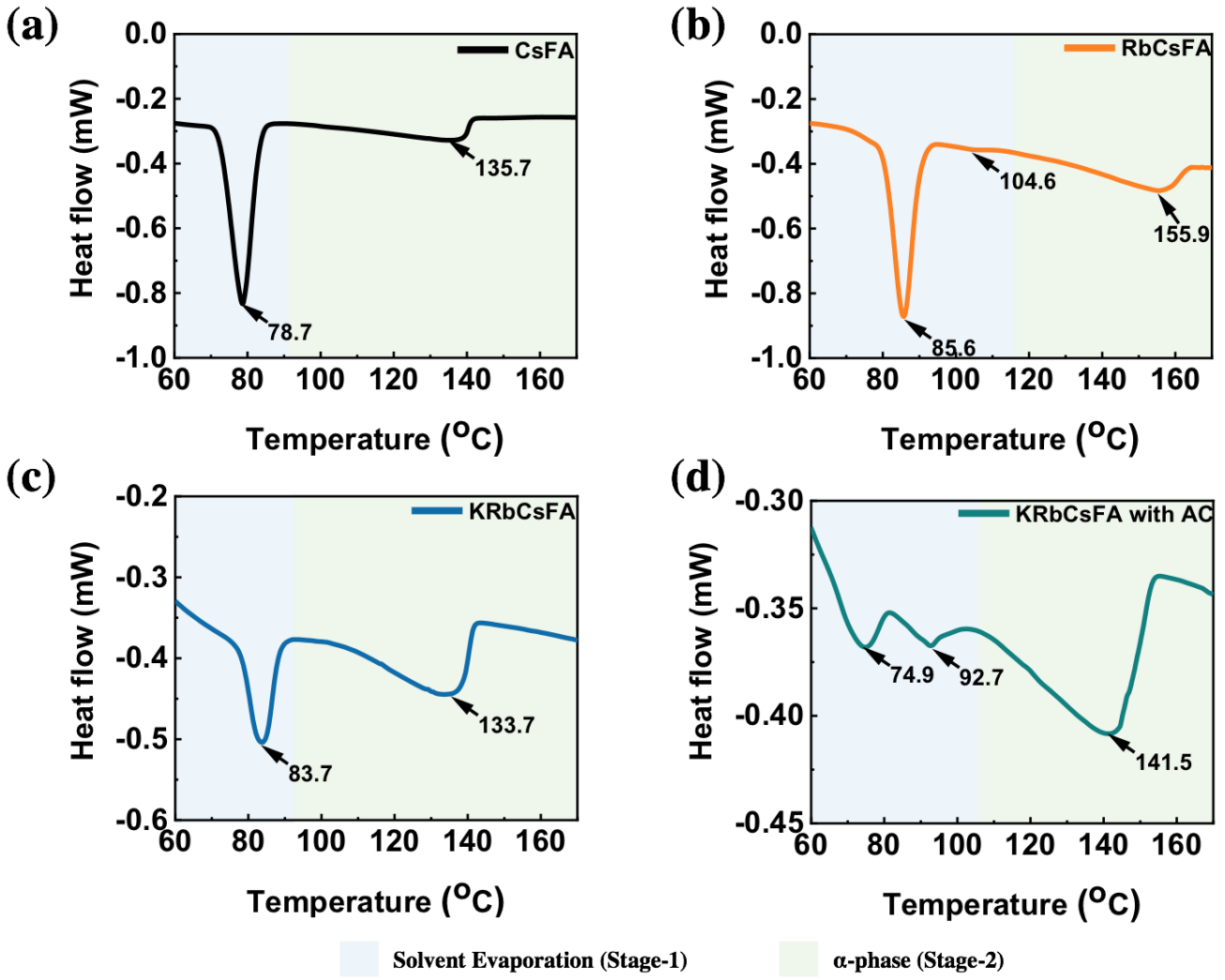

Figure 5. DSC curves of (a) CsFA, (b) RbCsFA, (c) KRbCsFA and (d)KRbCsFA/AC samples.

To verify that AC additive makes the m-AMCs distribution in KRbCsFA/AC sample more uniform, we systematically studied the film formation mechanism upon the annealing process through the combination of differential scanning calorimetry (DSC) (**Figure 5**) and GD-OES (**Figure 6** and **Figure S20**, Supporting Information) measurements. DSC was first employed to understand the effect of K, Cs, Rb, ammonium and chloride ions on the formation of the crystallized perovskite. The curves were measured on the four samples (CsFA, RbCsFA, KRbCsFA and KRbCsFA/AC) prepared as powders adducts (**Figures 5)**, completed by a $FAPbI_3$ powder adduct (**Figure S21**, Supporting Information). A first endothermic peak was observed at ~70°C-90°C, assigned to the evaporation of

Cite this paper as: D. Zheng, T. Zhu, Y. Yan, Th. Pauporté, Adv. Energy Mater., (2022) 2103618. DOI:10.1002/aenm.202103618.

DMSO (DMF was eliminated upon washing the adducts by diethyl ether)[40] since DMSO mixed with PbI_2 has been shown to start to evaporate at a temperature as low as 75°C.[41] First, a higher peak temperature was found for $FAPbI_3$ (82.8°C) compared to the CsFA sample (78.7°C). It suggests that the presence of CsI weakens the DMSO bonding. The evaporation temperature increased by around 5-6 °C with Rb and K introduced into PPS. However, for the sample with AC, the behavior was more complex with a first endothermic peak at 74.9 °C (**Figure 5d**), of lower intensity and a second one at 92.7 °C. It shows that in the presence of AC, the solvent elimination range is spread. For the $FAPbI_3$ sample, an endothermic peak was observed at 100.8 °C (**Figure S21**, Supporting Information), which is attributed in the literature to the crystallization of the perovskite yellow δ-phase.[41,42]. We can also see this peak with a small intensity at 104.6 °C in RbCsFA samples (**Figure 5b**), while it is absent in the other samples. Combining the results of XRD and SEM showed in **Figure 2**, it can be concluded that good crystallinity requires slow solvent elimination. Above 105°C, an extended endothermic feature was found, assigned to the crystallization of the α-phase perovskite compounds. In the case of $FAPbI_3$, it extended up to 162°C with a minimum of 153.4°C. This minimum can be roughly taken as the temperature at which the crystallization and growth steps end and allows a clear comparison between the samples. Adding different metal cations and additives can greatly affect the temperature corresponding to this step. Adding CsI significantly reduced this temperature to 135.7 °C. Through thermodynamic calculation, we can also see that the Gibbs free energy becomes lower after doping a small amount of Cs into $FAPbI_3$.[27] Also, a low temperature was found for the KRbCsFA sample (minimum at 133.7°C). The reason why CsFA and KRbCsFA samples do not have a peak related to the δ-phase may be due to the period of the process of crystallization of the δ-phase is short, and then this peak was hidden by the process of crystallization of the α-phase. Therefore, in both cases (CsFA and KRbCsFA), fast crystallization and growth occur. On the other hand, both RbI (in RbCsFA sample) and NH_4Cl (in KRbCsFA sample) can delay and slow down the perovskite crystal growth and it favors the better distribution of m-AMCs, as shown by GD-OES (**Figures 4n** and **4q**). This effect of AC was also observed by *in-situ* microscopy in the case of $MAPbI_3$ perovskite by Dai et al..[43]

Cite this paper as: D. Zheng, T. Zhu, Y. Yan, Th. Pauporté, Adv. Energy Mater., (2022) 2103618. DOI:10.1002/aenm.202103618.

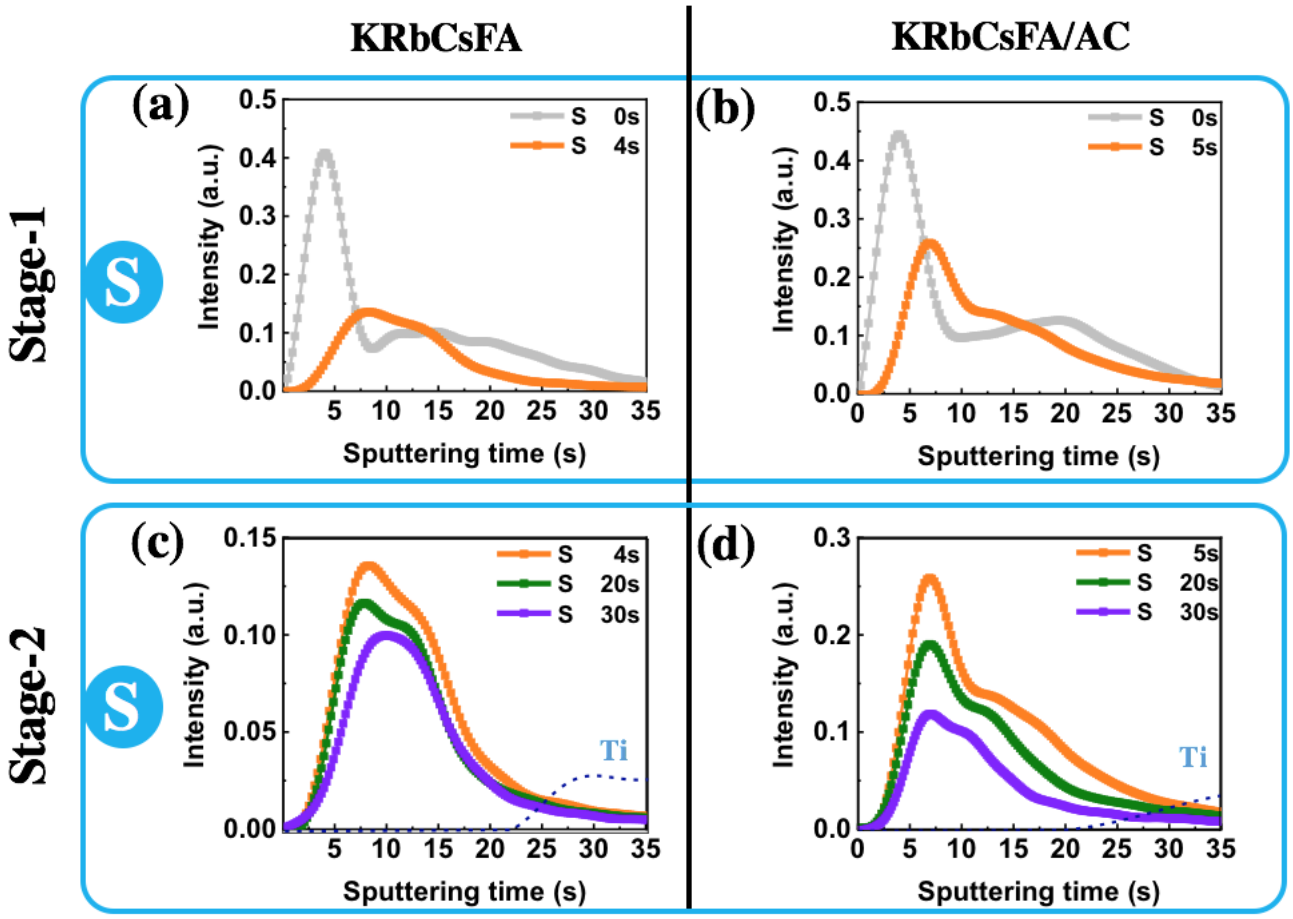

Figure 6. Evolution of GD-OES S (Sulfur) profile in the perovskite precursor layer upon annealing. (Dashed line in (c,d) is the Ti profile corresponding to the *meso*-TiO_2).

The residual solvent elimination is an essential aspect of the synthesis which occurs upon the film crystallization and growth. To our knowledge, some of us have been the first to use the GD-OES technique to follow the depth profile of the solvent leaving by evaporation upon the annealing of a perovskite film.[16] Indeed, the solvent employed in our experiments is a DMF-DMSO mixture and the S element contained in DMSO can be tracked by GD-OES. The S element profile for the various films and various annealing times are presented in (**Figures 6a-b** and **Figures S20**, Supporting Information**)**. With increasing the sputtering time, deeper part of the PVK layer is analyzed until reaching the *meso*-TiO_2 layer (dashed black line in **Figures 6a-b**). Before annealing, the DMSO profile is asymmetrical in every case, and we observe that the outer part of the film is more affluent in the solvent than the inner part.

For the annealing, our results distinguish two stages. The first one occurs during the first 4s-6s of thermal annealing on a hotplate. The initial film changes from yellow translucent to brown (**Figure S22**, Supporting Information). It is worth noting that the sample with AC added had the darkest color before annealing, which shows that the intermediate will undergo the phase change more easily. During

Cite this paper as: D. Zheng, T. Zhu, Y. Yan, Th. Pauporté, Adv. Energy Mater., (2022) 2103618. DOI:10.1002/aenm.202103618.

Stage-1, the most superficial residual solvent evaporates and is almost eliminated at the uttermost surface. Moreover, the four different initial wet layers are fully transformed into the α-phase (**Figure S23**, Supporting Information). The Stage-2 corresponds to 4-6s to 30s annealing time, when the film becomes dark-brown. We observed an apparent effect of m-AMCs and additives on the solvent distribution upon annealing. In the sample without AC, DMSO was eliminated fast near the surface, especially in sample CsFA (**Figure S20a**, Supporting Information) and KRbCsFA (**Figures 6a**). This result is in good agreement with the DSC result that both CsFA and KRbCsFA samples have a fast crystallization process. However, less solvent remained in the deeper part of the layer. For these three films, the solvent elimination profile evolution shows that the grains grow downward, from top to bottom. It favors the multiple and oblique grain boundaries and relatively small perovskite grains. The difference among these three samples is the rate of solvent evaporation from the top to the bottom. In the presence of RbI and KI in PPS, the S profiles are different compared to CsFA. For CsFA, the rate of the first peak reduction, which represents the layer near the surface, is faster than that of the second peak that represents the layer near the TiO_2 layer (**Figure S20c**, Supporting Information). This velocity difference makes it difficult for the inner solvent to evaporate so that the voids appear when the film formation process is completed (**Figure 2f**). If the perovskite grains in the upper layer are tightly bonded, it will be difficult for the solvent in the bottom part of the layer to pass through the perovskite in the upper layer and then to evaporate through the surface. Therefore, the remaining solvent will evaporate through pinholes and lateral diffusion. We believe that this is the actual reason for the formation of the voids. As for RbCsFA and KRbCsFA samples, the first peak drops faster than the second peak, but the gap between them is not as large as for the CsFA sample and the film produced is dense.

In the presence of AC, the profiles are different. For KRbCsFA/AC, the S profile is more extended throughout the layer thickness. Upon annealing, the solvent profile decreases uniformly throughout the layer thickness. It is deduced that a bulk grain lateral growth occurs in this case, resulting in more homogeneous films with big monolithic grains, as shown in the cross-section SEM image (**Figure 2f**). **Figure S24 (**Supporting Information) shows that the solvent was almost entirely eliminated after 2 min of thermal annealing for all the investigated samples. A striking result of this study is that the additive regulates the solvent elimination and then the growth of the film in its full depth. It boosts the quality of the film. In the above, by comparing the longitudinal distribution curves of K, Rb and Cs obtained at 30 s of thermal annealing for both KRbCsFA and KRbCsFA/AC samples, we concluded that the addition of AC could make the distribution of both Rb and Cs elements more uniform and finally leads to the improvement of the crystalline quality. Based on this, to compare the changes of m-AMCs lateral distribution after adding AC, we integrated the AMCs curves in **Figure 4o** and **Figure 4q**, and the obtained results are shown in **Figure S25** (Supporting Information). From the results, we can see that the integral area of AMCs was all improved substantially after the addition of AC. The more significant improvement is also an indication of the improved crystalline quality of the film. In summary, the combination of the results obtained in the transverse and longitudinal directions further

Cite this paper as: D. Zheng, T. Zhu, Y. Yan, Th. Pauporté, Adv. Energy Mater., (2022) 2103618. DOI:10.1002/aenm.202103618.

demonstrates that AC as an additive improves the film's crystalline quality by changing the film's growth direction.

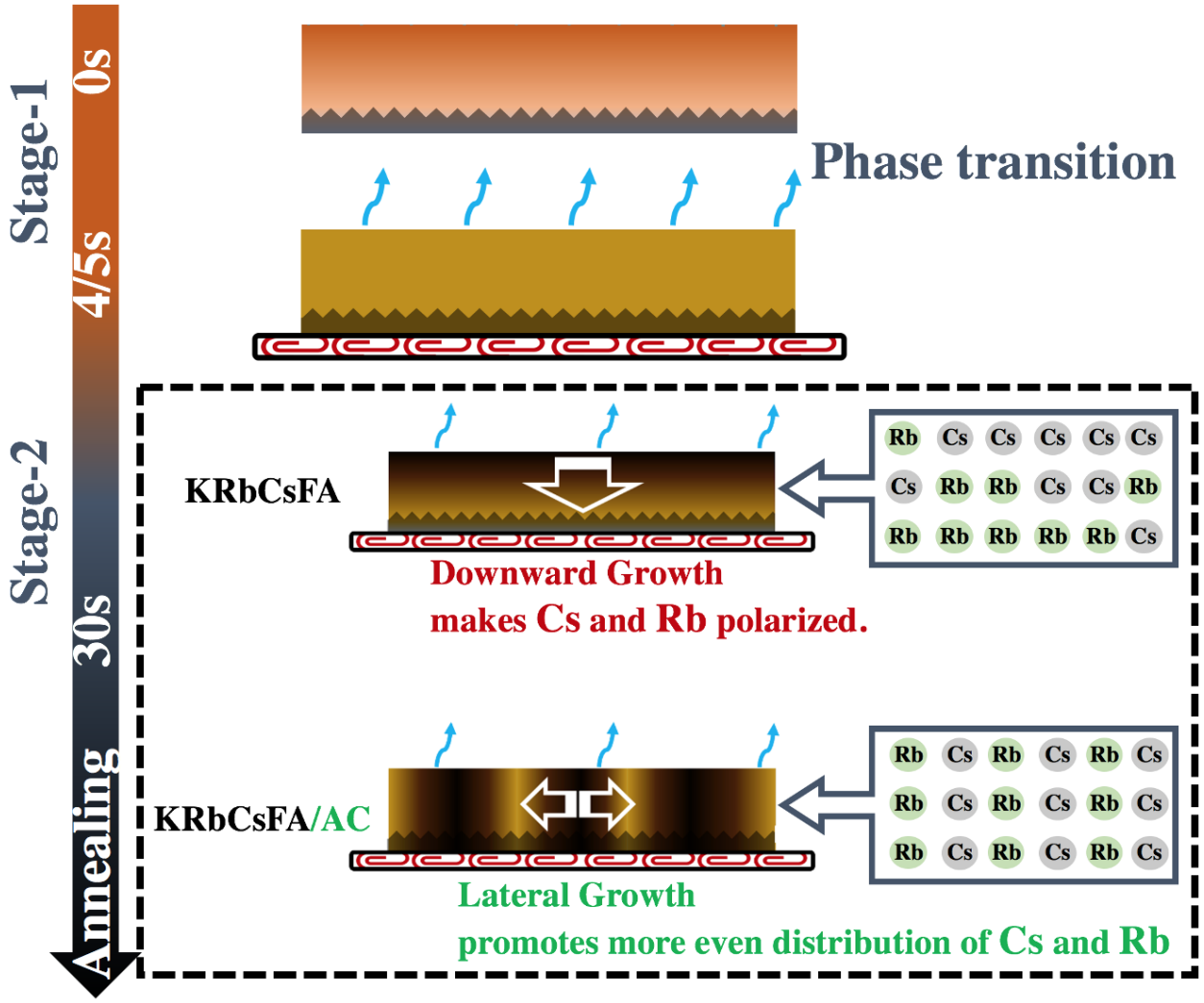

Figure 7. Schematic of the distribution of multi-cations in KRbCsFA perovskite layer prepared without and with AC and corresponding film formation process.

In **Figure 7**, we have summarized the grain growth mechanism linked to the solvent elimination and the trajectories of m-AMCs in the film formation process obtained by GD-OES and DSC techniques. We have unveiled the effect of m-AMCs on the film formation mechanism upon annealing. Two formation steps have been distinguished: first, the superficial residual solvent is eliminated, perovskite seed are formed and start to grow in all the directions. Second, the solvent in the depth of the film is evaporated. The elimination profile signs the final morphology of the layer. The downward (top-down) growth has been encountered for the CsFA, RbCsFA and KRbCsFA cases. It led to the formation of multiple boundaries and middle-sized grain morphology. We unveil that the KRbCsFA/AC sample employing potassium and ammonium chloride forces the homogeneous elimination of the solvent across the layer and then the lateral growth of the grains. It resulted in large

Cite this paper as: D. Zheng, T. Zhu, Y. Yan, Th. Pauporté, Adv. Energy Mater., (2022) 2103618. DOI:10.1002/aenm.202103618.

size (**Figure 2d**), monolithic and defect-poor grains with good coverage of the substrate, which are the targeted properties for high efficiency (**Figure 2f**). More importantly, this kind of film growth led to a more uniform distribution of Rb and Cs.

3. Conclusion

In summary, we have found the conditions for the preparation of perovskite layers with an homogeneous distribution of m-AMC, especially Rb^+. The mechanism of ammonium chloride action in m-AMCs perovskites, refined at each preparation process step, has been unveiled. Through a serious analysis, we found that ammonium chloride mainly leads to the formation of intermediates which can increase the solubility of PbI_2 and then favor the phase formation and transformation. Secondly, we explored the movement of m-AMCs in the perovskite layer during the film formation process by using the GD-OES technique and presented the intuitive evidence of phase segregation caused by potassium. We also confirmed that the atomic ratios change with the depth and that the targeted growth direction of the film is lateral growth. Finally, we combined this additive with GD-OES detection technology. We found how the additive influence the distribution of m-AMCs film formation and the formation of intersection layer between perovskite and TiO_2. We discovered that K at low concentration is homogeneously distributed throughout the film and does not accumulate at its surface. Cs are more concentrated at the surface and Rb in the film depth, but these two alkali metals are more homogeneously distributed with AC additive. We successfully prepared high-efficiency MA-free solar cells with a 21.1% PCE (stabilized at 20.8%) based on the above research results. Moreover, 22.53% PCE (stabilized at 22.04%) was achieved using a PAI post-treatment technique.

4. Experimental Section

Preparation of Substrate, Compact TiO_2, and Mesoporous TiO_2 layers:

Fluorine-doped SnO_2 (FTO) substrates (TEC 7 from Pilkington) were etched pattern by zinc powder and 10% HCl solution before being cleaned with soap and water. Subsequently, the substrates were immersed for 20 min in a concentrated 2.2M NaOH in ethanol/water (10:1 v/v %) and then rinsed with deionized water in an ultrasonic bath for 15 min. The substrates were subsequently heated at 500°C for 15 min. The compact TiO_2 hole blocking layer, noted *c*-TiO_2, was prepared by aerosol spray pyrolysis.[7] The TiO_2 nanoparticle solution employed to prepare the mesoporous layer, noted *mp*-TiO_2, was prepared in advance and stirred for at least 12h. The TiO_2 NR30-D paste (from Greatcell) was diluted in ethanol with a 1:7 w/w ratio. 45 µL of the solution was dropped on the *c*-TiO_2 layer and spin-coated at 2000 rpm for 15 s. The layer was then dried on a hotplate at 70 °C for 5-10 min and

Cite this paper as: D. Zheng, T. Zhu, Y. Yan, Th. Pauporté, Adv. Energy Mater., (2022) 2103618. DOI:10.1002/aenm.202103618.

finally heated at 500 °C under an air flux for 30 min, cooled down to 200 °C and removed from the hotplate.

Preparation of the PVK Layers:

$FAPbI_3$ layers preparation: 276.6 mg PbI_2 (1.2M, TCI) and 103.2 mg FAI (Greatcell) were mixed in 400 µL DMF and 100µL DMSO. For the sample with NH_4Cl (Alfa Aesar), we further add 9.6 mg NH_4Cl (Alfa Aesar) in the Perovskite Precursor Solution (PPS). The PPS was stirred for 2 h before use. The Spin-coating program was 1000 rpm for 10s and 4000 rpm for 30 s. 100 µL of chlorobenzene was dripped 20 s after the starting of the spinning routine. The layers were finally annealed on a hotplate at 155 °C for 15 min. These layers are denoted FA throughout the chapter.

$Cs_{0.10}FA_{0.90}PbI_3$ layers preparation: 253.6 mg PbI_2 (1.1M, TCI), 77.4 mg FAI (Greatcell) and 13.0 mg CsI (TCI) were mixed in 400 µL DMF and 100µL DMSO. For the sample with NH_4Cl (Alfa Aesar), we further add 8.0 mg NH_4Cl in the PPS. The PPS was stirred for 2 h before use. The Spin-coating program was 1000 rpm for 10s and 4000 rpm for 30 s. 100 µL of chlorobenzene was dripped 20s after the starting of the spinning routine. The layers were finally annealed on a hotplate at 155 °C for 15 min. These layers are denoted CsFA throughout the chapter.

$Rb_{0.05}Cs_{0.10}FA_{0.85}PbI_3$ layers preparation: 73.1 mg of FAI (Greatcell), 5.3 mg of RbI (Alfa Aesar), 12.9 mg of CsI (TCI) and 253.6 mg of PbI_2 (1.1M, TCI) were mixed in 100 µL DMSO and 400 µL DMF. For the sample with NH_4Cl (Alfa Aesar), we further add 8.0 mg NH_4Cl in the PPS. The PPS was stirred for a minimum of 2 h at room temperature in a N_2 filled glovebox before use. 30 µL of this solution was placed on top of the substrates. A two-step spin-coating program was employed: first spinning at 1000 rpm for 10 s and then at 4000 rpm for 30 s. 100 µL of chlorobenzene was dripped 20 s after the starting of the spinning routine. The films were then annealed at 155 °C for 15 min in glovebox with N_2 atmosphere. These layers are denoted RbCsFA throughout the chapter.

$K_xRb_{0.05}Cs_{0.10}FA_{0.85-x}PbI_3$ layers preparation: A mixed metal cation PPS was prepared by mixing FAI (68.8 mg (x=0.05)/ 64.5 mg (x=0.10)/ 60.2 mg (x=0.15), Greatcell), KI (4.2 mg (x=0.05)/ 8.3 mg (x=0.10)/ 12.5 mg (x=0.15), Sigma-Aldrich), 5.3 mg RbI (Alfa Aesar), 13.0 mg CsI (TCI) and 253.6 mg of PbI_2 (TCI) in 400 µL DMF and 100 µL DMSO to form $K_xRb_{0.05}Cs_{0.10}FA_{0.85-x}PbI_3$. For the $K_{0.05}Rb_{0.05}Cs_{0.10}FA_{0.80}PbI_3$ sample with NH_4Cl (Alfa Aesar), we further add 2.7 mg (10 mol %, noted AC-10), 5.4 mg (20 mol %, noted AC-20), 8.0 mg (30 mol %, noted AC-30) and 10.7 mg (40 mol %, noted AC-40) NH_4Cl in the PPS. The solutions were stirred for a minimum of 4h at room temperature in a nitrogen filled glovebox. 30 µL of this solution was placed on top of the substrates. A two-step spin-coating program was ran: first spinning at 1000 rpm for 10 s and then at 4000 rpm for 30 s. 100 µL of chlorobenzene was dripped 20 s after the starting of the spinning routine. The films were then annealed at 155 °C for 15 min. The PAI post-deposition treatment consisted in dropping 60 µL of a 4 mg/mL n-propylammonium chloride (PAI) solution onto the cooled perovskite film. A one-step spin-

Cite this paper as: D. Zheng, T. Zhu, Y. Yan, Th. Pauporté, Adv. Energy Mater., (2022) 2103618. DOI:10.1002/aenm.202103618.

coating program was started just after dropping: 2000 rpm/s acceleration, 3000rpm for 20s. These $K_{0.05}Rb_{0.05}Cs_{0.10}FA_{0.80}PbI_3$ without (with) NH_4Cl layers are denoted KRbCsFA (KRbCsFA/AC) throughout the chapter.

The hole transporting material (HTM) solution was prepared by dissolving 78 mg of Spiro-OMeTAD (Borun New Material Technology) in 1 mL of chlorobenzene. Then, 17.9 µL of bis(trifluoromethylsulfonyl)imide lithium salt solution (Li-TFSI) (Sigma Aldrich) solution (517 mg in 1 mL ACN), 30.4 µL of TBP (tert-butylpyridine) (Sigma Aldrich) and 14 µL of tris(2-1H-pyrazol-1-yl)-4-tert-butylpyridine)-cobalt(III) tris (bis(trifluoromethylsulfonyl)imide) (Dyesol, FK209) (376 mg in 1 mL acetonitrile) were added to this solution. 40 µL of the HTM solution was spin-coated at 4000 rpm for 30 s. Finally, the device was completed by thermally evaporating a 70-80 nm thick gold back contact on the Spiro-OMeTAD layer.

Synthesis of adduct powders: First, 0.5 mL of precursor solutions were prepared by using the recipe mentioned above. Second, 10 mL of diethyl ether was added to precipitate the corresponding adduct. The precipitates were collected and dried in N_2 filled Glovebox overnight.

Characterization methods

The structure of the organometal lead perovskite films was characterized by a PANanalytical X-Pert high-resolution X-ray diffractometer (XRD) operated at 40 kV and 45 mA and using the CuKα radiation with λ= 1.5406 Å. The film specular absorbance was measured by a Cary 5000 UV-Vis-NIR spectrophotometer. A glass/FTO/*c*-TiO_2/*mp*-TiO_2 sample was employed for the baseline. The photoluminescence spectra were measured by a Cary Eclipse fluorescence spectrophotometer. The morphology of perovskite thin films was measured using a field-emission SEM equipment (Zeiss Supra 40) in the in-lens mode. Glow-Discharge Optical Emission Spectrometry (GD-OES) analyses were performed using a HORIBA Jobin Yvon GD Profiler 2 equipment. This instrument was equipped with a RF-generator (at 13.56 MHz), a standard HORIBA Jobin Yvon glow discharge source with a cylindrical anode of 4 mm internal diameter and two optical spectrometers (a polychromator and a monochromator) for fast-optical detection. The Ar plasma was generated at an Ar pressure of 420 Pa and an applied power of 17 W. The precursor or perovskite layer or the solar cell was mounted on an O-ring at one side of the plasma chamber and used as a cathode. The *J-V* curves were recorded by a Keithley 2410 digital sourcemeter, using a 0.1 $V.s^{-1}$ voltage scan rate. The solar cells were illuminated with a solar simulator (Abet Technology Sun 2000) filtered to mimic AM 1.5G conditions (100 mW/cm^2). The illuminated surface was delimited by a black mask with an aperture diameter of 3 mm. The power density was calibrated at 100 $mW.cm^{-2}$ by the use of a reference silicon solar cell.[11] The tracking experiments were performed under ambient conditions. The current was followed at the voltage of the maximum power. The external quantum efficiency (*EQE*) spectra were measured using an Oriel QUANTX-300 system. The light beam was chopped at 77Hz. The monochromatic illumination was calibrated by a NIST-calibrated Si photodiode. The sample morphologies were

examined with a high resolution Ultra 55 Zeiss FEG field-emission scanning electron microscope (FE-SEM) in the in-lens mode.

Acknowledgements

Dr. Philippe Vermaut (IRCP, Chimie-paristech, France) is acknowledged for giving us access to the DSC 3 apparatus from STAR System. The Ph.D scholarship of D. Zheng was funded by the CSC-Paristech program (grant number 201806310126). The ANR agency is acknowledged for financial support via the Moreless project ANR-18-CE05-0026 and the ChemSta project ANR-21-CE05-0022.

References

[1] M. M Lee, J. Teuscher, T. Miyasaka, T. N. Murakami, H. J. Snaith, *Science* **2012**, *338*, 643-647.

[2] H.-S. Kim, C.-R. Lee, J.-H. Im, L. K.-B. Lee, T. Moehl, A. Marchioro, S.-J. Moon, R. Humphry-Baker, J.-H. Yum, J. E. Moser, M. Grätzel, N.-G. Park, *Sci. Rep.* **2012**, *2*, 591.

[3] J. Burschka, N. Pellet, S.-J. Moon, R. Humphry-Baker, P. Gao, M. K. Nazeeruddin, M. Grätzel, *Nature* **2013**, *499*, 316.

[4] H. Zhou, Q. Chen, G. Li, S. Luo, T. Song, H.-S. Duan, Z. Hong, J. You, Y. Liu, Y. Yang, *Science* **2014**, *345*, 542-546.

[5] J. Zhang, P. Barboux, T. Pauporté, *Adv. Energy Mater.* **2014**, *4*, 1400932.

[6] J. Zhang, E. J. Juárez-Pérez, I. Mora-Seró, B. Viana, Th. Pauporté, *J. Mater. Chem. A* **2015**, *3*, 4909–4915.

[7] P. Wang, Z. Shao, M. Ulfa, T. Pauporté, *J. Phys. Chem. C* **2017**, *121*, 9131–9141.

[8] T. Zhu, J. Su, F. Labat, I. Ciofini, Th. Pauporté *ACS Appl. Mater Interfaces* **2020**, *12*, 744-752.

[9] F. Zhang, K. Zhu, *Adv. Energy Mater.* **2020**, 10, 1902579.

[10] A. Leblanc, N. Mercier, M. Allain, J. Dittmer, V. Fernandez, T. Pauporté, *Angew. Chem. Int. Ed.* **2017**, *56*, 16067 –16072.

[11] D. Pitarch-Tena, T.T. Ngo, M. Vallés-Pelarda, T. Pauporté, I. Mora-Seró. *ACS Energy Lett.* **2018**, *3*, 1044−1048.

[12] NREL Chart (January 2022) https://www.nrel.gov/pv/cell-efficiency.html

[13] N. Pellet, P. Gao, G. Gregori, T.Y. Yang, M.K. Nazeeruddin, J. Maier, M. Gratzel, *Angew. Chem. Int. Ed.* **2014**, *53*, 3151− 3157.

[14] T. Zhu, D. Zheng, J. Liu, L. Coolen, T. Pauporté, *ACS Appl. Mater. Interfaces* **2020**, *12*, 37197−37207.

[15] Z. Li, M.J. Yang, J.S. Park, S.H. Wei, J.J. Berry, K. Zhu, *Chem. Mater.* **2016**, *28*, 284−292.

[16] D. Zheng, T. Pauporté, *J. Mater. Chem. A* **2021**, *9*, 17801-17811.

[17] Y.H. Park, I. Jeong, S. Bae, H.J. Son, P. Lee, J. Lee, C. Lee, M.J. Ko, *Adv. Funct. Mater.* **2017**, *27*, 1605988−16059815.

[18] M. Saliba, T. Matsui, J.Y. Seo, K. Domanski, J.P. Correa-Baena, M.K. Nazeeruddin, S.M. Zakeeruddin, W. Tress,

Cite this paper as: D. Zheng, T. Zhu, Y. Yan, Th. Pauporté, Adv. Energy Mater., (2022) 2103618. DOI:10.1002/aenm.202103618.

A. Abate, A. Hagfeldt, M. Gratzel, *Energy Environ. Sci.* **2016**, *9*, 1989−1997.

[19] T. Duong, H.K. Mulmudi, H.P. Shen, Y.L. Wu, C. Barugkin, Y.O. Mayon, H.T. Nguyen, D. Macdonald, J. Peng, M. Lockrey, W. Li, Y.B. Cheng, T.P. White, K. Weber, K. Catchpole, *Nano Energy* **2016**, *30*, 330−340.

[20] M.A. Mahmud, N.K. Elumalai, M.B. Upama, D. Wang, A.M. Soufiani, M. Wright, C. Xu, F. Haque, A. Uddin, *ACS Appl. Mater. Interfaces* **2017**, *9*, 33841-33854.

[21] D. Zheng, T. Zhu, T. Pauporté, *Solar RRL* **2021**, *5*, 2100010.

[22] J.-P. Correa-Baena, Y. Luo, T.M. Brenner, J. Snaider, S. Sun, X. Li, M. A. Jensen, N.T. Putri Harton, L. Nienhaus, S. Wieghold, J.R. Poindexter, S. Wang, Y. S. Meng, T. Wang, B. Lai, M. V. Holt, Z. Cai, M. G. Bawendi, L. Huang, T. Buonassisi, D. P. Fenning, *Science* **2019**, *363*, 627–631.

[23] W.S. Yang, J.H. Noh, N.J. Jeon, Y. Kim, S. Ryu, J. Seo, S.I. Seok, *Science* **2015**, *348*, 1234–1237.

[24] S.S. Shin, E.J. Yeom, W.S. Yang, S. Hur, M.G. Kim, J. Im, J. Seo, J.H. Noh, S.I. Seok, *Science* **2017**, *356*, 167–171.

[25] W.S. Yang, B.-W. Park, E.H. Jung, N.J. Jeon, Y.C. Kim, D.U. Lee, S.S. Shin, J. Seo, E.K. Kim, J. Noh, S.I. Seok, *Science* **2017**, *356*, 1376–1379.

[26] M. Abdi-Jalebi, Z. Andaji-Garmaroudi, S. Cacovich, S. Camille, P. Bertrand, M.R. Johannes, A. Mejd, P.B. Edward, M.H. Eline, J.P. Andrew, L. Samuele, J.S. Tom, R. Hakan, D. Giorgio, D. Caterina, H.F. Richard, D.S. Samuel, *Nature* **2018**, *555*, 497–501.

[27] B. Philippe, M. Saliba, J. Correa-Baena, B. Cappel, S. Cruz, M. Graẗzel, A. Hagfeldt, H. Rensmo. *Chem. Mater.* **2017**, *29*, 3589−3596.

[28] G. Tong, X. Lan, Z. Song, G. Li, H. Li, L. Yu, J. Xu, Y. Jiang, Y. Sheng, Y. Shi, K. Chen, *Mater. Today Energy* **2017**, *5*, 173-180.

[29] G. Tong, D.Y. Son, L. K. Ono, Y. Liu, Y. Hu, H. Zhang, A. Jamshaid, L. Qiu, Z. Liu, Y. Qi, *Adv. Energy Mater.* **2021**, 2003712.

[30] Y. Rong, X. Hou, Y. Hu, A. Mei,L. Liu, P. Wang, H. Huang, *Nat. Commun.* **2017**, *8*, 14555.

[31] S. Turren-Cruz, A. Hagfeldt, M. Saliba, *Science* **2018**, *362*, 449-453.

[32] S. Li, Z. Liu, Z. Qiao, X. Wang, L. Cheng, Y. Zhai, Q. Xu, Z. Li, K. Meng, G. Chen, *Adv. Funt. Mat.* **2020**, *30*, 2005846.

[33] M. Zhang, J. Bing, Y. Cho, Y. Li, J. Zheng, C.F.J. Lau, M.A. Green, S. Huang, A. Ho, *Nano Energy* **2019**, *63*, 2211-2855.

[34] Y. Guo, K. Shoyama, W. Sato, Y. Matsuo, K. Inoue, K. Harano, C. Liu, H. Tanaka, E. Nakamura, *J. Am. Chem. Soc.* **2015**, *137*, 15907−15914.

[35] D.S. Dolzhnikov, H.J. Zhang, J. Jang, M.G. Son, T. Panthani, S. Shibata, D.V. Chattopadhyay, *Science* **2015**, *347*, 425-428.

[36] G.E. Eperon, G. M. Paterno, R.J. Sutton, A. Zampetti, A.A. Haghighirad, F. Cacialli, H.J. Snaith, *J. Mater. Chem. A* **2015**, *3*, 19688.

[37] R.J. Sutton, G.E. Eperon, L. Miranda, E. Parrott, B.A. Kamino, J.B. Patel, M.T. Hörantner, M. Johnston, A.A. Haghighirad, D.T. Moore, H.J. Snaith, *Adv. Energy Mater.* **2016**, *6*, 1502458.

[38] D.M. Trots, S.V. Myagkota, *J. Phys. Chem. Solids* **2008**, *69*, 2520.

Cite this paper as: D. Zheng, T. Zhu, Y. Yan, Th. Pauporté, Adv. Energy Mater., (2022) 2103618. DOI:10.1002/aenm.202103618.

[39] N. Li, Y. Luo, Z. Chen, X. Niu, X. Zhang, J. Lu, R. Kumar, J. Jiang,H. Liu, X. Guo, B. Lai, G. Brocks,Q. Chen, S. Tao, D.P. Fenning, H. Zhou, *Joule*, **2020**, *4*, 1743-1758.

[40] G. Grancini, C. Roldán-Carmona, C.I. Zimmermann, E. Mosconi, X. Lee, D. Martineau, S. Narbey, F. Oswald, F. De Angelis, M. Graetzel, M.K. Nazeeruddin, *Nature Commun.* **2017**, *8*, 15684.

[41] W.S. Yang, J.H. Noh, N.J. Jeon, Y.C. Kim, J. Ryu, S. Seo, S.I. Seok, *Science* **2015**, *348*, 1234.

[42] J.-W. Lee, D.-J Seol, A.-N Cho, N.G. Park, *Adv. Mater.* **2014**, *26*, 4991-4998.

[43] X. Dai, Y. Deng, C.H. Van Brackle, S. Chen, N. Peter, X. Rudd, Y. Xiao, B. Chen, J. Huang, *Adv. Energy Mater.* **2020**, *10*, 1903108.

Cite this paper as: D. Zheng, T. Zhu, Y. Yan, Th. Pauporté, Adv. Energy Mater., (2022) 2103618. DOI:10.1002/aenm.202103618.

Graphical abstract